

Front-End ASIC for the STROBE-X HEMA and WFM Detectors: Concept and Design

Gianluigi De Geronimo^{a,b,c,*}, Paul S. Ray^d, Eric A. Wulf^d, Colleen A. Wilson-Hodge^e, Eric Burns^f, Yuri Evangelista^g, Anthony Hutcheson^d, Thomas J. Maccarone^h, Gianluigi Zampaⁱ

^aNuclear Engineering and Radiological Sciences, University of Michigan, Ann Arbor, MI 48109, USA

^bElectrical and Computer Engineering, Stony Brook University, Stony Brook, NY 11794, USA

^cDG Circuits, dgcircuits.com, Syosset, NY 11973, USA

^dSpace Science Division, U.S. Naval Research Laboratory, Washington, DC 20375 USA

^eAstrophysics Branch, NASA's Marshall Space Flight Center, Huntsville, AL 35812, USA

^fLouisiana State University, Dept. of Physics and Astronomy, 202 Nicholson Hall, Baton Rouge, LA, 70803, USA

^gINAF - Istituto di Astrofisica e Planetologia Spaziali, Via del Fosso del Cavaliere 100, 00133, Roma, Italy

^hDepartment of Physics & Astronomy, Texas Tech University, Box 41051, Lubbock, TX, 79409-1051, USA

ⁱIstituto Nazionale di Fisica Nucleare (INFN), Trieste TS, Italy

Abstract. This paper presents the NSX front-end ASIC, being developed to read charge signals from the HEMA and WFM X-ray detectors for the STROBE-X mission. The ASIC reads out signals from up to 64 anodes of linear Silicon Drift Detectors (SDDs). When unloaded, the ASIC channel has a charge resolution, expressed in Equivalent Noise Charge (ENC) of about $2.8 e^-$. Once connected to the SDD anode we anticipate, for the 80 keV energy range, a ENC of about $10.7 e^-$ at a leakage current of 2 pA, which corresponds to a FWHM of about 145 eV at 6 keV once the Fano-limited statistics from charge generation in Si is included. The acquisition is event-triggered and, for events exceeding the threshold, the ASIC measures the peak amplitude and stores it in an analog memory for subsequent readout. The ASIC can also force the measurement of the sub-threshold channels neighboring the triggered channel, including the ones that belong to neighbor chips by using bi-directional differential inter-chip communication. Alternatively, the ASIC can measure the amplitudes of all channels at the time of the first detected peak. Additional features include a high-resolution option, channel power down and skip function, a low-noise pulse generator, a temperature sensor, and the monitoring of the channel analog output and trimmed threshold. The power consumption of the individual channel is $\sim 590 \mu\text{W}$ and, when including all shared circuits, it averages to $\sim 670 \mu\text{W}$ / channel.

Keywords: ASIC, Low-Noise, X-ray, Silicon Drift Detector, STROBE-X.

* Gianluigi De Geronimo, E-mail: degeronimo@ieee.org

1 Introduction

STROBE-X (Spectroscopic Time-Resolving Observatory for Broadband Energy X-rays) is a NASA probe-class observatory designed to perform X-ray spectroscopy and timing over a broad range of energies (200 eV to 80 keV) and timescales (microseconds to years). It is part of a large multi-messenger astronomy program aiming at studying the matter in the most extreme conditions found in the universe.¹⁻⁴ As shown in Fig. 1a, STROBE-X is composed of three instruments: a $\sim 1.6 \text{ m}^2$ soft-band (0.2 to 12 keV) Low Energy Modular Array (LEMA), a $\sim 3.4 \text{ m}^2$ hard-band (2 to 30 keV, and up to 80 keV in extended mode) High Energy Modular Array (HEMA), and a $\sim 1,456 \text{ cm}^2$ hard-band (2 to 50 keV) Wide Field Monitor (WFM). Details on the architecture and purpose of each instrument can be found in other papers in this Volume.⁴⁻⁷

The HEMA and WFM instruments of interest to the work presented in this paper are based on linear Silicon Drift Detectors (SDDs)⁸⁻¹¹ where the anodes are arranged in a single fine pitch row with drift lines parallel to each other and the charge is collected along one edge of the sensor, as shown in Fig. 1b. The SDD design is optimized for X-ray astronomy to achieve a $450 \mu\text{m}$ depletion with a sensitive energy range up to 80 keV.

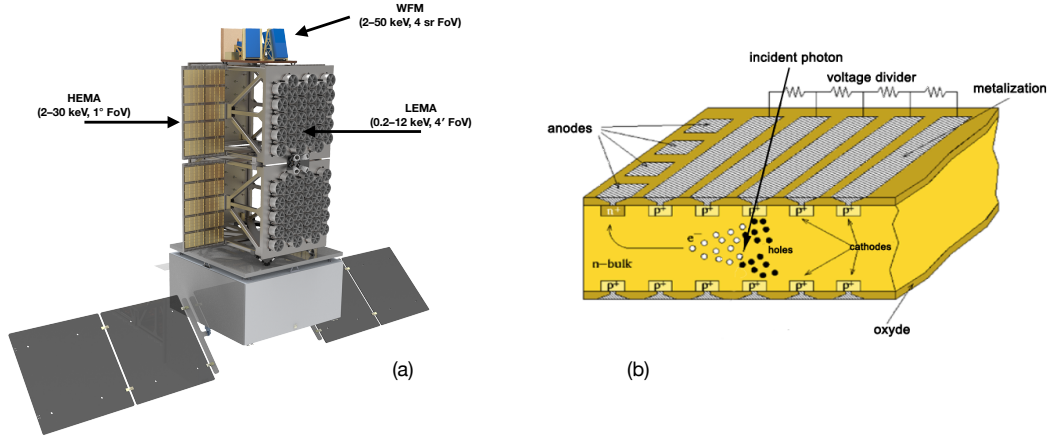


Fig 1 (a) STROBE-X observatory concept showing the LEMA, HEMA, and WFM instruments and (b) working principle of the linear Silicon Drift Detector (SDD).

Each individual HEMA SDD has an active area of 70 mm in the drift direction and 108.5 mm in the equipotential direction. The drift direction is segmented in two halves of 35 mm each with the highest voltage along the central symmetry axis, and the charge is collected at the two opposite edges with 112 anodes on each side spaced $970 \mu\text{m}$. The estimated event multiplicity (i.e. the number of triggered adjacent strips per event from charge sharing) is between one and two. Eight 14-channel low-noise Application-Specific Integrated Circuits (ASICs) provide the readout of each half independently for a total of 16 ASICs per detector. As shown in Fig. 2a, each individual HEMA module is composed of 4×4 of such detectors and capillary plate collimators with a 70% open area ratio. The modules are then assembled in four panels, where each panel includes $5 \times 2 = 10$ modules (Fig. 1a) for a total of 40 modules covering a total area of $\sim 4.86 \text{ m}^2$. When taking into account the collimators, the effective sensitive area is reduced to $\sim 3.4 \text{ m}^2$.

Each individual WFM SDD has a size of 70 mm in the drift direction and 64.9 mm in the equipotential direction, realizing almost a square. Like the HEMA, the drift direction is segmented in two halves of 35 mm each with the highest voltage along the central symmetry axis, and the charge is collected at the two opposite edges with 384 anodes on each side spaced $169 \mu\text{m}$. The estimated event multiplicity is between one and eight. Six 64-channel ASICs provide the readout of each half independently for a total of 12 ASICs per detector. As shown in Fig. 2b each individual WFM module is composed of 2×2 detectors, a $25 \mu\text{m}$ thick Beryllium window to prevent the direct impact of micro-meteorites and small orbital debris particles, and a coded mask. Eight WFM modules are assembled in four pairs where, for each pair, the two modules are placed orthogonal to each other in order to obtain precise two-dimensional (2D) source positions from the combined information. The total sensitive area of the 8 WFM camera modules is $\sim 1,453 \text{ cm}^2$.

With regards to the front-end ASIC for the HEMA and WFM instruments, the relevant specifications and requirements are summarized in Table 1. The requirements on the FWHM include the Fano-limited statistics from charge generation in Si at 6 keV. The requirements on the charge resolution, expressed in Equivalent Noise Charge (ENC), include a $\sim 20\%$ safety margin. We anticipate that at the beginning of life the instruments will comfortably meet the requirements, while towards the end of life due to the increased leakage current from SDD degradation, low temperatures down to -55° combined with short peaking times may be needed, with the possible drawback of some

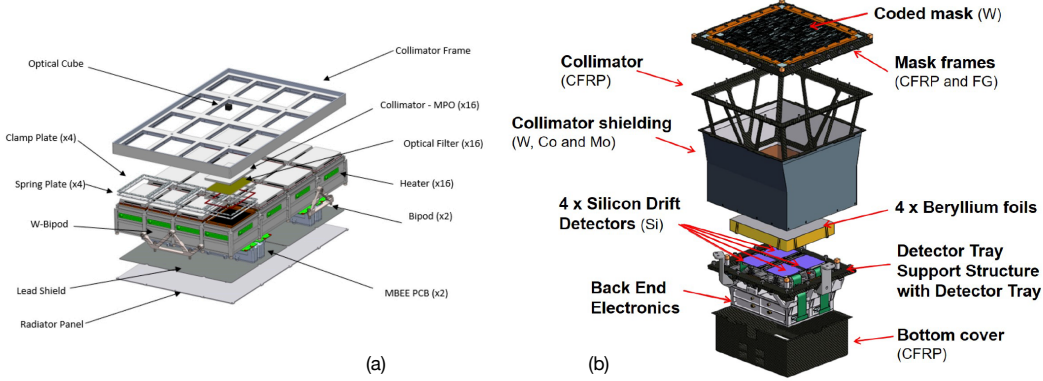


Fig 2 Exploded CAD drawing of (a) an individual HEMA module and (b) and single WFM camera.

ballistic deficit.

Table 1 Front-end electronics specifications and requirements for each instrument.

Parameter	HEMA	WFM
Anode Capacitance	90 fF	80 fF
Anode Pitch	970 μm	169 μm
Number of Anodes per Half Detector	112	384
Number of Electronic Channels per ASIC	14	64
Wirebond Interconnect Capacitance [†]	40 fF	30 fF
Minimum Leakage Current	7 pA	2 pA
Maximum Leakage Current	300 pA	90 pA
Triggered Anodes per Event (Event Multiplicity)	1 to 2	1 to 8
Maximum Event Rate per Channel [‡]	15 cps	5 cps
Energy Resolution FWHM at 6 keV in Si [◇]	200 eV	300 eV
Equivalent Noise Charge per Channel [‡]	15 e ⁻	13 e ⁻
Maximum Power Consumption per Channel	650 μW	720 μW
Maximum Energy	up to 80 keV [§]	
Energy Threshold [‡]	~470 eV	
Charge Drift Time	$\leq 2.2 \mu\text{s}$	
Charge Collection Time at Anode	$\leq 160 \text{ ns}$	
Operating Temperature	-55 °C to +35 °C	
Radiation Tolerance TID	10 krad	

[†] estimated values; [‡] including event multiplicity

[◇] for single-anode events; [§] extended mode⁶

This paper is organized as follows: in Section 2 we discuss the ASIC architecture and functionality, and in Section 3 we discuss the CMOS technology, the physical layout, the planned interconnects, and we present selected post-layout transistor-level simulations.

2 ASIC Architecture

The architecture of the first ASIC prototype is shown in Fig. 3 with the individual channel enclosed in the dashed rectangle. Optimized for the WFM instrument, it includes functionality and

programmability that will allow its initial use with the HEMA instrument as well. Design modifications to optimize the ASIC for the HEMA instrument, especially to limit the power consumption, will be done at a later time.

The ASIC integrates 64 channels, each composed of a dual-stage low-noise charge amplifier, a shaper (sh) with baseline stabilizer, an event discriminator with trimmable threshold (trm), a peak detector (pd), control logic, and a configuration register. Shared among channels are the neighbor logic, multiplexers, bias circuits, two DACs to control the threshold and test pulse generator amplitudes, shared configuration registers, and a temperature sensor.

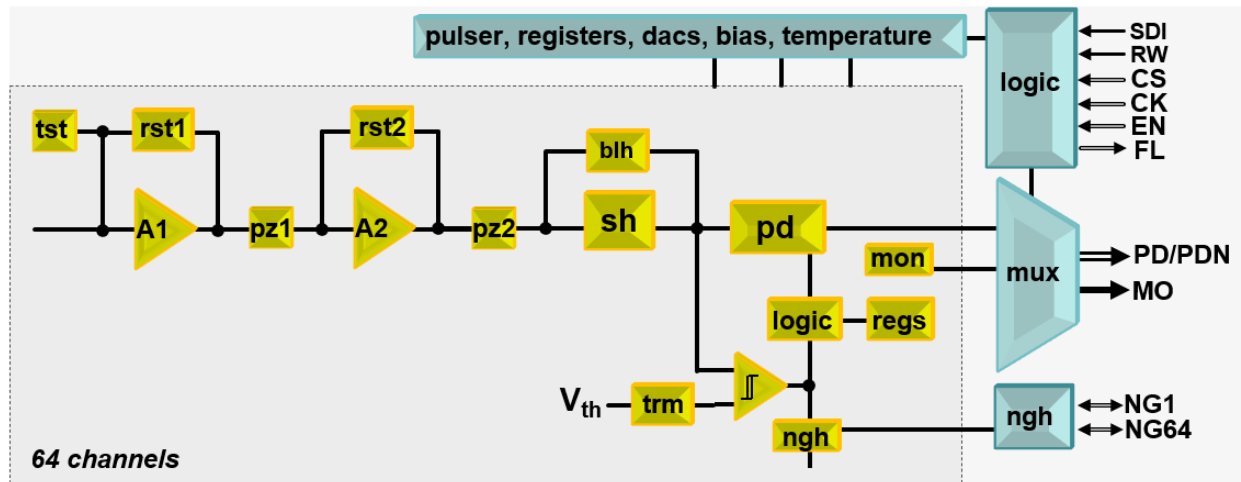


Fig 3 Block diagram illustrating the NSX ASIC architecture (acronyms specified in §2).

2.1 Charge Amplifier

The input MOSFET is an optimized¹² p-channel with gate size $L/W = 270 \text{ nm} / 40 \mu\text{m}$ ($4 \times 10 \mu\text{m}$ fingers) biased at a Drain current $I_D = 62 \mu\text{A}$ and a $V_{DS} = 440 \text{ mV}$ (saturation voltage $V_{DSAT} \approx 90 \text{ mV}$), resulting in a gate capacitance $C_G \approx 73 \text{ fF}$ and a transconductance $g_m \approx 890 \mu\text{S}$ with a sub-threshold slope coefficient $n \approx 1.33$ and an inversion coefficient $\gamma \approx 0.59$. Including the low-frequency noise, with a coefficient $K_f \approx 0.64 \times 10^{-24} \text{ J}$ and a slope $\alpha_f = 1.064$,¹³ the MOSFET can yield a ENC of about $2.8 e^-$ rms without load, and a slope on the order of $2.6 e^-$ per 100 fF of input load at a peaking time of $1 \mu\text{s}$. The user has the option of increasing the Drain current to $I_D = 170 \mu\text{A}$ for a $g_m = 1.68 \text{ mS}$ yielding $\sim 2.6 e^-$ unloaded with a slope of $\sim 3.1 e^-$ per 100 fF of input load at a peaking time of 500 ns, which may be beneficial in case of high detector leakage current (high parallel noise), although at expenses of some ballistic deficit and the additional power consumption from the increased Drain current. For the trace, wirebond pad, and bond wire, we estimate a total capacitance on the order of 65 fF, to be added to the SDD anode capacitance. Once connected to the SDD anode, a resolution of $\sim 10.7 e^-$ ($\sim 145 \text{ eV FWHM}$ at 6 keV once the Fano-limited statistics from charge generation in Si is included) is anticipated at a leakage current of 2 pA for the energy range of $\sim 80 \text{ keV}$ (see simulations in §3.2), which corresponds to an analog dynamic range, defined as ratio between the maximum charge and the ENC, in excess of 880.

The charge amplifier (A1, rst1, pz1) implements a continuous mirror reset¹⁴ with p-channel MOSFETs of size $L/W = 20 \mu\text{m} / 220 \text{nm}$ and $\sim 10 \text{fF}$ Metal-Oxide-Metal (MOM) capacitors, capable of self-adapting to leakage currents from $\sim 15 \text{fA}$ to $\sim 500 \text{pA}$, and providing through the pole-zero compensation (pz1)¹⁴ a linear charge gain of 32. A programmable bias current of either 1 pA or 20 pA, realized using scaling mirrors, can be enabled to emulate the leakage current from the sensor when needed (e.g. when the sensor is either not biased or not connected to the channel). The second stage of the charge amplifier (A2, rst2, pz2), similar but with the input MOSFET operating at lower bias current and with feedback based on Metal-Insulator-Metal (MIM) capacitors, provides an additional linear charge gain programmable to either 32 or 64, resulting in a total charge gain of either 1,024 or 2,048, needed to minimize the noise contribution from the shaper and the following stages. Overall, after the shaper, a charge-to-voltage conversion gain of either ~ 400 or $\sim 800 \text{mV/fC}$ is achieved to cover, with the available voltage swing of 1.5 V, maximum energies of $\sim 84 \text{keV}$ and $\sim 42 \text{keV}$ respectively. For test purposes, an injection capacitor (tst) of 10 fF (MOM) connected to the integrated shared pulse generator can be enabled. The power consumed by the two charge amplifier stages is $\sim 110 \mu\text{W}$.

2.2 Shaper and Baseline Stabilizer

The shaper (sh) is a 3rd order with complex-conjugate poles realized using the delayed dissipative feedback (DDF) configuration,¹⁵ with peaking time programmable to 0.25, 0.5, 1, and 2 μs and characterized by noise coefficients $A_{\text{vw}} = 0.85$, $A_{\text{vf}} = 0.54$ and $A_{\text{iw}} = 0.61$ for white series, $1/f$ series and white parallel contributions respectively (unilateral noise power spectral densities).¹² The baseline stabilizer is based on the baseline holder configuration,¹⁶ it provides a non-linear high-pass filter with a small-signal -3dB frequency on the order of 1 kHz, and it sets the shaper output baseline to $\sim 150 \text{mV}$ using a band-gap referenced voltage characterized by high rejection against process and temperature variations. Particular attention has been paid to guarantee high stability vs temperature and detector leakage current (see post-layout simulations in §3.2). The power consumed by the shaper plus stabilizer is $\sim 248 \mu\text{W}$.

2.3 Discrimination

The discriminator is based on a comparator, a trimmer (trm), and logic. The comparator is designed to achieve a hysteresis of about 5 mV to discriminate signals as low as $\sim 280 \text{eV}$ in the 84 keV range, which is lower than the required $\sim 470 \text{eV}$ for worst-case event multiplicity. The trimmer allows per-channel adjustment in $\sim 800 \mu\text{V}$ steps ($\sim 22.5 \text{eV}$ at the maximum conversion gain) for a total of $\sim 12 \text{mV}$ (4 bit per channel). The coarse threshold can be adjusted using a shared 10-bit DAC in $\sim 800 \mu\text{V}$ steps over a range from 0 V to $\sim 820 \text{mV}$. The noise contribution from the entire discriminator is on the order of 200 μV rms. The power consumed by the comparator plus the trimmer DAC and amplifier is $\sim 38 \mu\text{W}$.

Events that exceed the threshold are processed for peak detection as described later. The user has the option to force the acquisition and processing of the two channels neighbor to the channel exceeding the threshold. This includes channels that belong to a neighbor chip, where chips communicate event occurrence to each other using two bi-directional LVDS interfaces (one per neighbor chip).¹⁷ Additionally, the user has the option to force the acquisition and processing of all channels in the same chip once a channel exceeds the threshold. Two options allow the user to disable the discrimination either after a first channel exceeds the threshold or after a first channel

finds the peak amplitude. These last two options have been introduced to limit, when needed, the impact of pick-up from digital activity.

2.4 Peak Detection

The peak detector (pd) provides the extraction and storage of the peak amplitude of the shaped pulse. The circuit is based on the offset-free error-cancellation concept^{18,19} and it operates in three consecutive phases, as illustrated in the simplified schematic of Fig. 4.

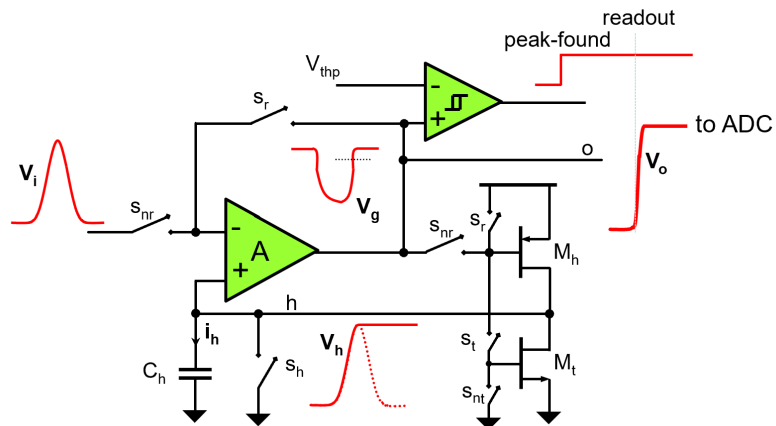


Fig 4 Simplified schematic illustrating the three-phase operation of the peak detector circuit.

When the acquisition starts (i.e. after the circuit has been reset by briefly closing the switch s_h), the circuit is configured for tracking-mode where the switch s_t is closed (and the complement s_{nt} open), the switches s_r are open (and the complements s_{nr} closed), and the hold node h continuously tracks the baseline of the analog shaper, including noise. The tracking is affected by errors from the offset-voltage and finite common-mode rejection of the amplifier A . When the shaped pulse exceeds the event threshold (or, optionally, when other channels force the acquisition as discussed earlier), the circuit changes its configuration to peak-detect-mode where the switch s_t is open (and the complement s_{nt} closed) while the hold node h continues tracking the rising part of the analog pulse until it reaches the maximum amplitude (peak). Since there is no discharge path for the node h , the peak value is held on the hold capacitor C_h . The user can program the channel to detect either the first occurring peak or the highest peak within the same acquisition time window. After the peak is found, the circuit switches its configuration into read-mode, where the switches s_r are closed (and the complements s_{nr} open) and the amplifier is reconfigured to operate as a unity-gain buffer for the readout of the voltage stored in the hold capacitor C_h . While the voltage held at the node h is affected by errors from the offset-voltage and finite common-mode rejection of the amplifier, the buffered voltage available at the output node o has these errors cancelled. This is possible due to the re-usage of the same amplifier during all three consecutive phases.¹⁸ Particular attention has been paid to guarantee high accuracy at all amplitudes, including the ones very close to the discrimination threshold (see simulations in §3.2).

When the peak is found, a peak-found signal is generated (see Fig. 4), OR-ed with the peak-found signals from all other channels. The result of the OR function is a shared peak-found signal occurring at the first peak-found event among all channels. Following the shared peak-found a flag

is released by the ASIC with a ~ 400 ns delay, alerting the external control logic that one or more above-threshold events have been (or are being) processed. The control logic stops the acquisition after a pre-determined time and starts the multiplexed readout, as described in the next subsection. The pre-determined time is a system-level variable controlled by the user which takes into account the maximum time difference between events of interest within the same acquisition. If enabled, an option forces all channels to store the voltage in correspondence of the first peak-found. This option has been added to allow measurement and possibly subtraction of common-mode pick-up, if present. The power consumed by the peak-detection circuit is $\sim 80 \mu\text{W}$.

2.5 Acquisition and Readout

The external data acquisition system (DAQ) drives the ASIC digital control signals EN (enable), CS (chip-select) and CK (clock), and receives from the ASIC the digital signal FL (flag). The ASIC enters the Acquisition mode by asserting EN. In Acquisition mode the channels become sensitive to events. Events that exceed the threshold (and, if configured for those options, either the sub-threshold neighbors or all other sub-threshold channels) are processed for peak detection. Once a peak is found, the ASIC asserts the FL and, after a pre-determined time, the DAQ stops the Acquisition by lowering EN. Next, the ASIC enters the Readout mode by asserting CS. Once in Readout mode, the ASIC generates an internal digital token signal, which can be transferred to the first channel at the falling edge of a CK pulse. Once the token reaches the first channel, the FL becomes a channel-event indicator for that channel. If FL is high, the channel needs to be read out and the stored peak amplitude of that channel is made available at the analog output PD to be converted by an external analog-to-digital converter (ADC). A rising edge of CK will change the purpose of the FL signal, which now becomes the threshold-crossing indicator for that channel, providing information whether or not the channel exceeded the threshold. Once the ADC sampling is complete the DAQ can move the token to the next channel by providing an additional CK pulse. Channels which present a low FL are empty channels and do not need to be read out. For those empty channels, the token can stop for a much shorter time than the case where the peak amplitude needs to be read out and converted. The readout sequence is repeated until all 64 channels have been scanned and, when needed, converted. The channel identifier associated with each conversion is derived from the number of CK pulses. Once all 64 channels have been scanned, CS can be de-asserted and the ASIC enters a short acquisition-reset cycle and becomes ready for a new Acquisition-Readout sequence.

Assuming conservatively an event multiplicity of 8, a 10 MHz CK, and a 1 MS/s ADC (e.g. the space-rated version of the LTC2378), a worst-case readout time on the order of $14 \mu\text{s}$ can be achieved. Considering that each half-detector operates independently and does not measure during a readout, a non-paralyzable analysis can be performed in order to calculate, given the dead time, the per-channel output count rate (OCR) vs input count rate (ICR). The result, shown in Fig. 5, assumes a worst-case peaking time of $2 \mu\text{s}$, the worst-case event multiplicity, and it takes into account that the ASICs in each half detector would be read out in parallel. From Fig. 5 it can be observed that the proposed architecture can satisfy the rate requirement for both the HEMA and WFM instruments with a maximum event loss of $\sim 0.8\%$ and $\sim 2.8\%$ respectively. In the extreme case where all the channels need to be read out (e.g. to subtract common-mode pick-up), the readout time will exceed $64 \mu\text{s}$ and the HEMA and WFM instruments will suffer a maximum

event loss of $\sim 2.5\%$ and $\sim 11\%$ respectively. For such cases, ADCs with shorter conversion time may be considered.

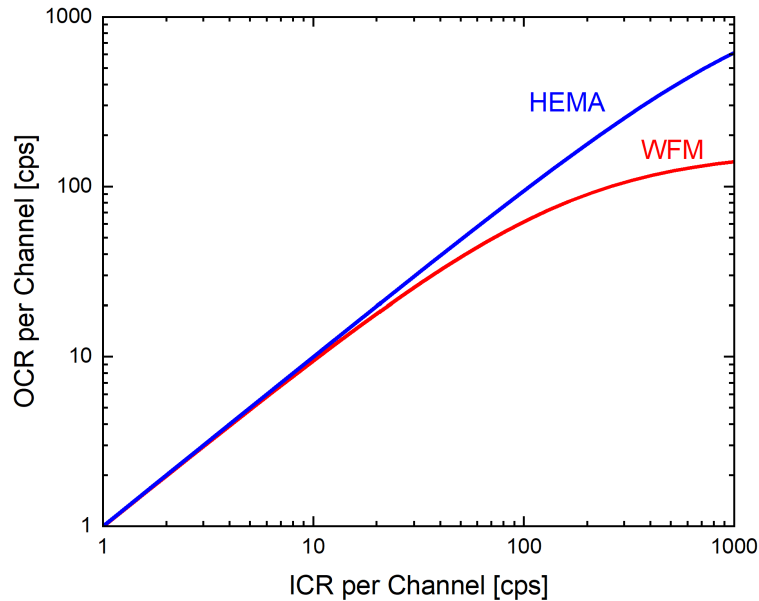


Fig 5 Calculated per-channel Output Count Rate (OCR) vs Input Count Rate (ICR). At the required maximum count rate, the corresponding event loss for the HEMA and WFM instrument would be 0.8% and 2.8% respectively.

Depending on the power budget, available CK frequency, and ADC conversion speed, architectures where ADCs are shared among multiple ASICs may be adopted. Additionally, a channel that has been powered down by configuration will be skipped by the token during the readout process, thus reducing the number of channels to be scanned. This functionality can be particularly useful when the ASIC is used to read out the signals from the HEMA detector, where only 14 channels are needed out of 64.

2.6 Interfaces, Additional Functionality, Total Power Consumption-colored, and Radiation Tolerance

The analog interface includes, along with the 64 sensitive inputs, the two analog outputs PD and MO. The peak-detector output PD allows the readout of the stored analog peak amplitudes during readout. It also includes a programmable buffer capable of driving several hundreds of pF with a sub-200 ns settling time. Optionally, the user can enable a second buffered output PDN to have a fully differential and buffered output signal. The monitor output MO can be configured to measure various internal analog signals. The user can monitor, for each individual channel, either the shaper output or the trimmed threshold. The user can also monitor the voltage of the ~ 1.24 V integrated bandgap reference, the ~ 150 mV analog baseline reference, the output of the 10-bit DAC which sets the untrimmed event threshold, the output of the 10-bit DAC which sets the amplitude of the integrated pulse generator, and the output of an integrated temperature sensor which has a nominal response of ~ 924.5 mV + ~ 3.27 mV/ $^{\circ}$ C.

The complete digital interface includes two CMOS inputs (SDI, RW) for the configuration, three LVDS inputs (CS, CK, EN) for the control of the acquisition and readout, one low-power

LVDS output (FL) for the event/channel flag which requires an external 1 k Ω termination, and two low-power LVDS bi-directional lines (NG1, NG64) used by neighbor ASICs to communicate threshold events to each-other and do not require termination.

A combination of the CK, RW and CS signals allows the user to generate either a soft reset, which optionally resets all acquisition circuits in preparation of a new acquisition, or a hard reset which performs the full ASIC reset including the configuration.

In normal (non-high-resolution) mode the channel power consumption is $\sim 590 \mu\text{W}$. In high-resolution mode the power consumption increases to $\sim 890 \mu\text{W}$. In power down mode the channel consumption reduces to $\sim 90 \mu\text{W}$. The shared circuits consume up to $\sim 6 \text{ mW}$ depending on the configuration. The total power consumption in normal configuration is on the order of 43 mW (i.e. $\sim 670 \mu\text{W}$ per channel).

The configuration registers are designed using the Dual Interlocked Storage Cell (DICE),²⁰ which has high tolerance to Single Event Upsets (SEU). The anticipated Total Ionizing Dose (TID), lower than 10 krad, does not represent a concern for the selected CMOS technology.²¹

3 CMOS Technology, Physical Layout and Post-Layout Simulations

The design is in a well-established commercial mixed-signal 180 nm CMOS technology selected for its anticipated long-term availability, reliable models, and affordable fabrication costs in shared and dedicated runs. The technology has also been extensively modeled and characterized for operation at room and cryogenic temperature.¹³

3.1 Physical Layout and Interconnections

The physical layout of the first ASIC prototype, with a size of 3.4 mm \times 10.2 mm, is shown in Fig. 6a. The aspect ratio is within the 3:1 recommended to guarantee die integrity during die saw. The 64 inputs are located on the left side of the die, while the rest of the interface (supplies, grounds, analog and digital signals) is located on the right side.

Each channel measures 1.9 mm \times 136 μm plus the interconnect and round-shaped input pad (Fig. 6b). The parasitic capacitance of the pad, characterized by an opening diameter of 40 μm suitable for 1 mil bond wire and realized using the two uppermost metal layers (M5 and M6), plus the metal interconnect is on the order of 25 fF. The channels are grouped in eight (Fig. 6b) with a pad pitch of 136 μm and inter-group spacing rails of 136 μm . The spacing rails and the two top and bottom rails are used to bring the charge amplifier supply from the right side to the left side of the ASIC. In Fig. 6b the input MOSFET is also visible, surrounded by a yellow rectangle.

The right side of the ASIC layout is dedicated to the shared circuits and to pads for the supplies, grounds, analog and digital interfaces, with a minimum pad pitch of 170 μm . The uppermost and lowermost differential pads (NG) provide the bi-directional inter-chip communication for neighboring as described in the previous section. The PS pads provide the dedicated 1.8 V for the charge amplifier supply (Source of the input MOSFET), the AS and AG pads provide the 1.8 V to 0 V analog supply and ground. The digital interface is localized at the center, surrounded by the DS and DG pads which provide the 1.8 V to 0 V digital supply and ground.

Fig. 7 shows the planned wirebond drawing for both the WFM case and, for initial testings, the HEMA case. In the WFM case, where the anode pitch is 169 μm , the spacing between adjacent chips covering 64 SDD anodes will be in excess of 500 μm , after subtracting $\sim 30 \mu\text{m}$ for the seal ring and $\sim 80 \mu\text{m}$ for the scribe line (saw street). In the HEMA case, where the anode pitch is

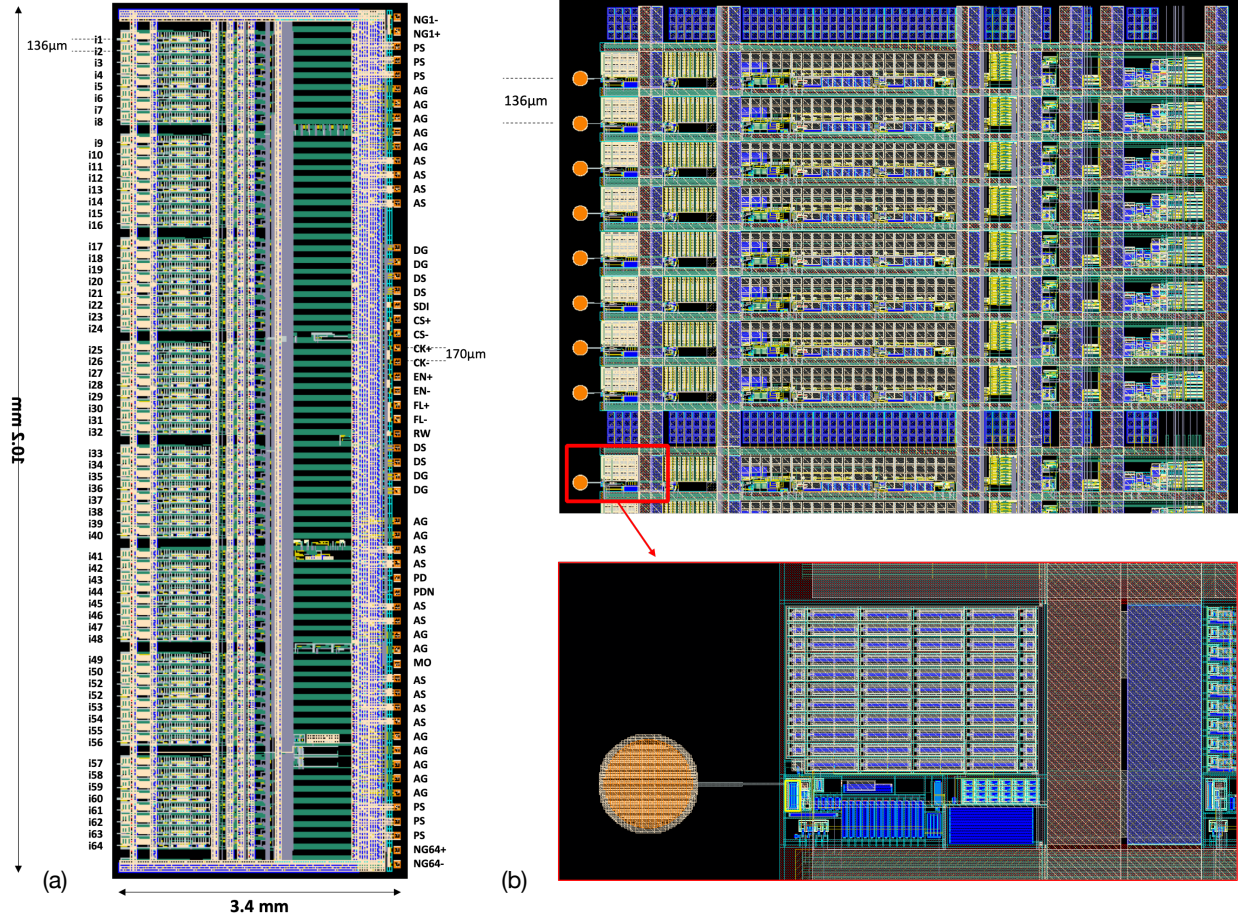


Fig 6 Physical layout of (a) the NSX ASIC and (b) of a group of 8 channels with zoomed detail of the input.

970 μm , the spacing between adjacent chips covering 14 SDD anodes will be on the order of 3.2 mm. The die will be positioned in order to have a maximum bond wire angle of 45 degrees and a maximum bond wire length of ~ 3.6 mm, with an estimated worst case parasitic capacitance on the order of 40 fF.

3.2 Transistor-Level Simulations

The design has been extensively simulated transistor-level using the industry-standard CAD tools from Cadence Design Systems, with pre- and post-layout netlists where the latter includes the extracted parasitic capacitances associated with the physical layout. Fig. 8 shows the extracted ENC at the four peaking times for the energy ranges of the 80 keV, 40 keV and 40 keV high-res (i.e. with the high-resolution mode enabled). This simulation assumes the WFM case and a leakage current of 2 pA. The shot noise associated with the detector leakage current is included. For comparison, the theoretical ENC is also shown, along with the three dominant contributions (white series, $1/f$ series, and white parallel). The theoretical curves include the noise contributions from the stages following the charge amplifier, and which amounts to $\sim 5\%$ of the total ENC.

The simulated analog response vs temperature to an input charge $Q_{\text{in}} = 2$ fC (signal current modeled using an approximate Dirac δ function) is shown in Fig. 9a, along with the conversion

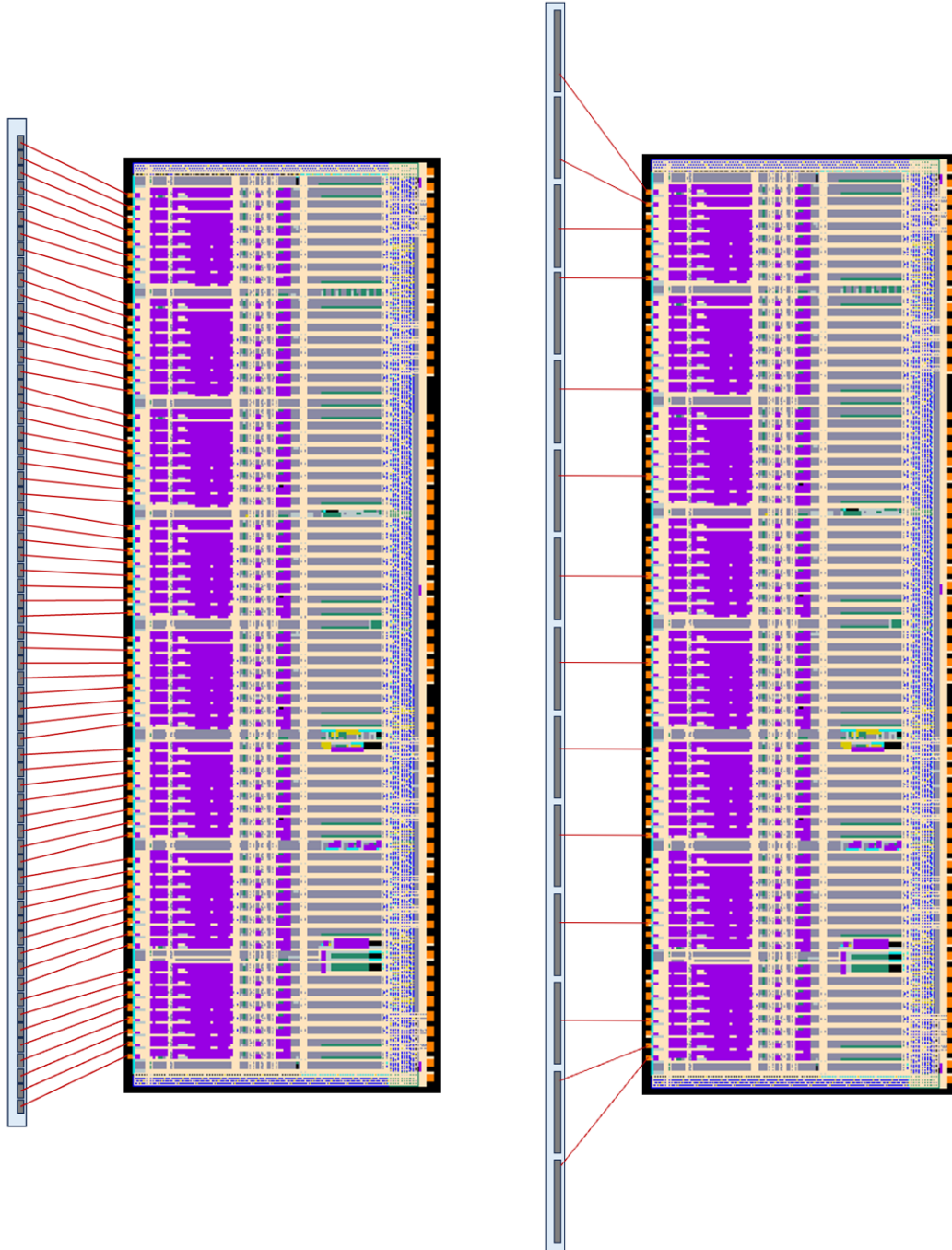


Fig 7 Planned wire bonding drawing for the WFM case (left, 64 anodes at 169 μm pitch) and, for initial testings, the HEMA case (right, 14 anodes at 970 μm pitch). A maximum wire bond angle of 45° is maintained.

gain and output baseline (Fig. 9b), for temperatures from $-60\text{ }^{\circ}\text{C}$ to $+40\text{ }^{\circ}\text{C}$. A gain change on the order of 0.5% can be observed over the entire temperature range.

Similarly, the simulated analog response vs detector leakage current to an input charge $Q_{\text{in}} = 2\text{ fC}$ ($\sim\delta$ Dirac current) is shown in Fig. 10a, along with the gain and output baseline (Fig. 10b), for leakage currents from 1 pA to 400 pA.

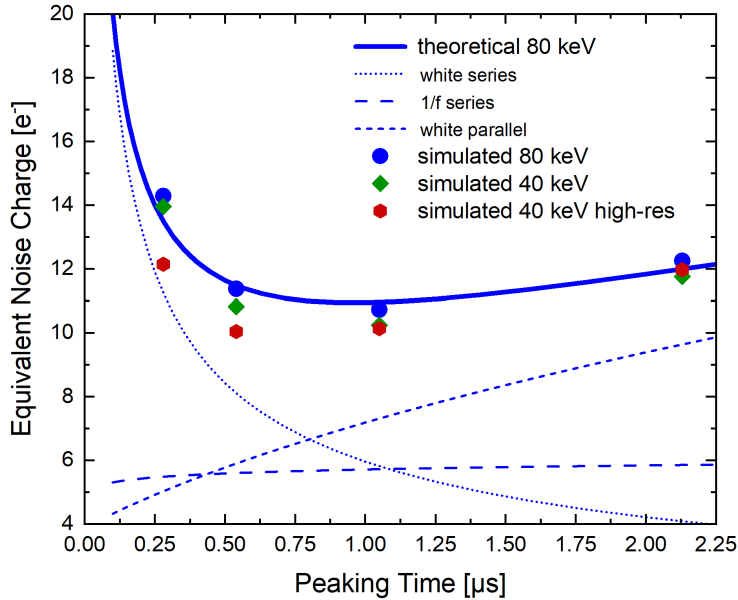


Fig 8 Theoretical and simulated Equivalent Noise Charge for the WFM case at the nominal leakage current.

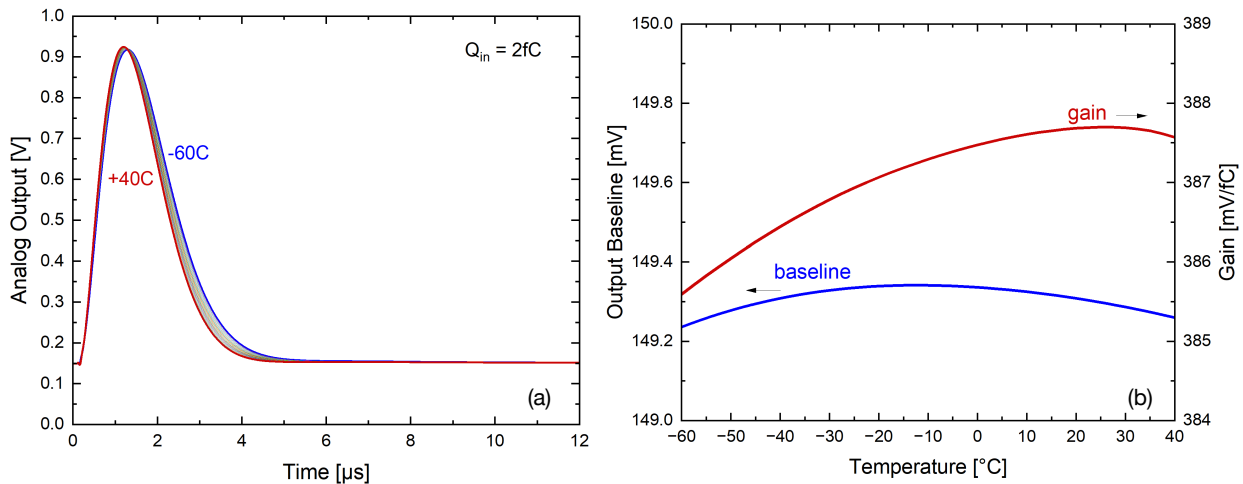


Fig 9 Simulated analog response to 2 fC (a) and baseline and conversion gain (b) vs temperature.

In Fig. 11a the simulated peak detector response and accuracy are shown at 1 μ s peaking time, for input charges from 36 aC (\sim 810 eV) to 3.6 fC (\sim 81 keV). A relative error on the order of 2.75 mV can be observed, which corresponds to less than 0.2% over the full range. Taking into account the linear component, an error well below 0.1% can be expected.

A simulation example of a complete acquisition and readout sequence is shown in Fig. 12. In this example the discrimination threshold is set to \sim 400 mV, and events occur in channels 1, 2, 10 and 11 where the latter does not exceed the threshold. The signals EN, FL, CS, CK and NG (inter-chip) are also shown, in digital form. For this simplified example, a single readout clock frequency of 2.5 MHz has been adopted.

The sequence starts with setting EN high. Once the events occur and the first peak is found the

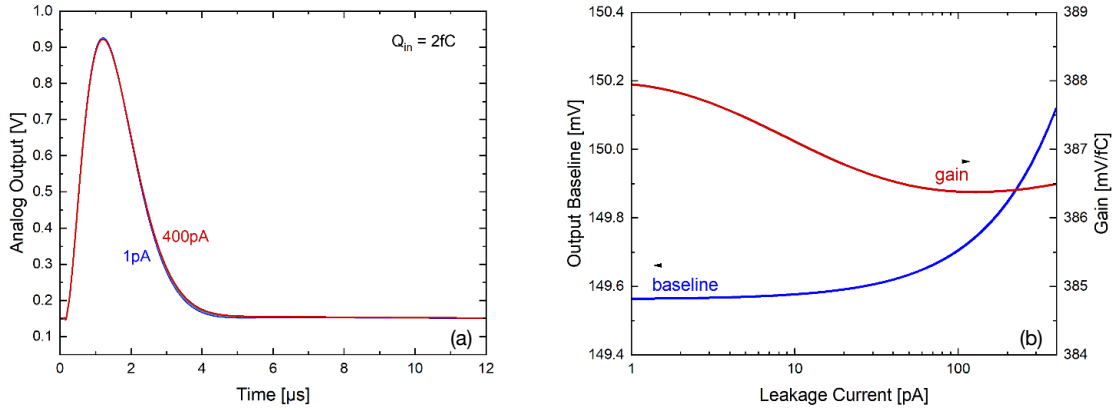


Fig 10 Simulated analog response to 2fC (a) and baseline and gain (b) vs detector leakage current.

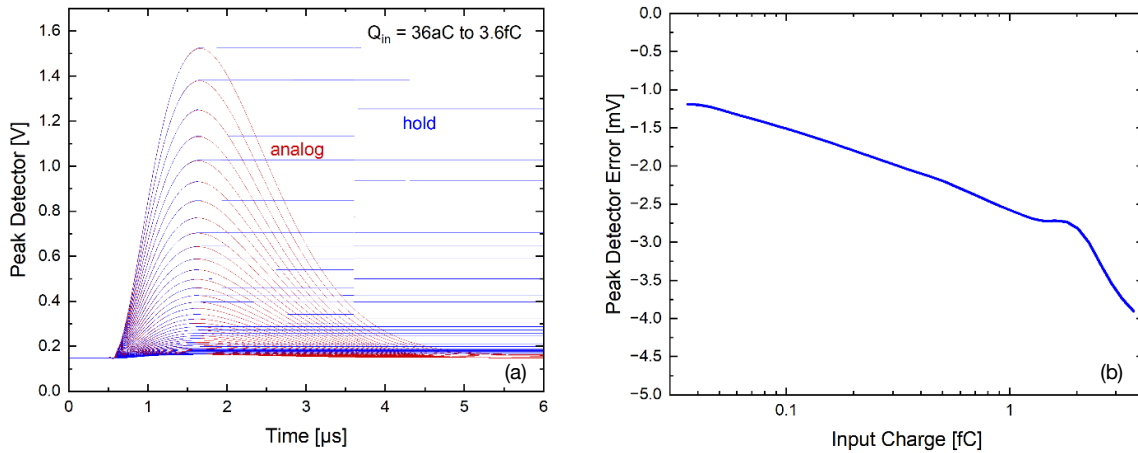


Fig 11 Simulated peak detector response (a) and accuracy (b) vs input charge Q_{in} .

ASIC releases, with a ~ 400 ns delay, the FL. The DAQ de-asserts EN, asserts CS and generates the sequence of CK. At the first falling edge of CK the high FL indicates that channel 1 needs to be converted and the PD output presents its peak amplitude. At the next rising edge of CK the high FL indicates that channel 1 exceeded the threshold. At the second CK cycle the same happens for channel 2. At the third CK cycle the sub-threshold neighbor channel 3 is read out, with amplitude close to the baseline, and at the falling edge of CK the FL is de-asserted indicating that channel 3 did not exceed the threshold. The next 21 CK cycles indicate no events until channels 25, 26, and 27 where both 25 and 27 did not exceed the threshold. The inter-chip neighboring signal occurs at the threshold crossing of channel 1.

Disclosures

The authors have no potential conflicts of interest to disclose.

Code, Data, and Materials Availability

Data sharing is not applicable to this article, as no new data were created or analyzed.

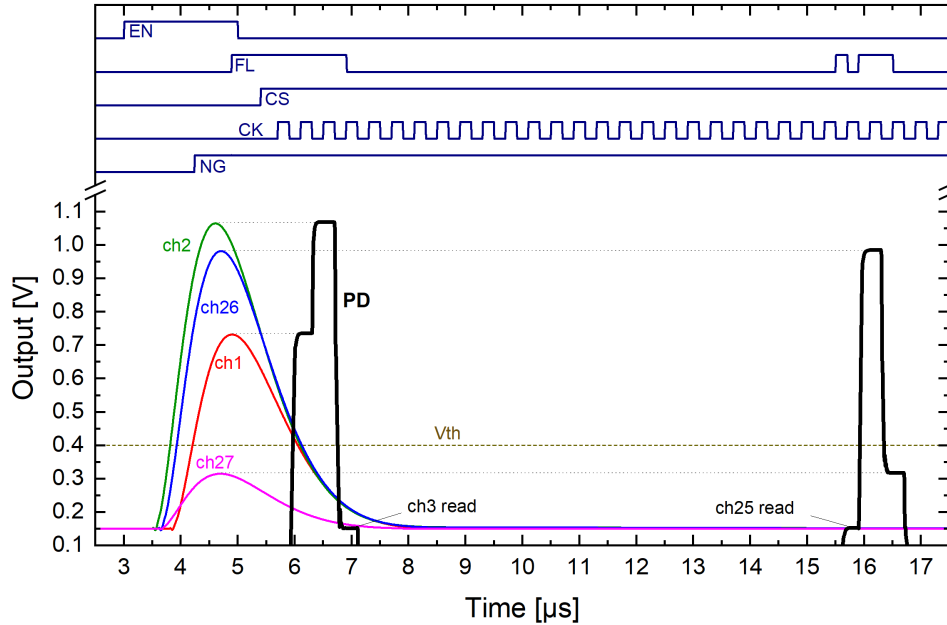


Fig 12 Example of a full acquisition and readout cycle.

Acknowledgments

The authors are very grateful to Marco Feroci (National Institute of Astrophysics (INAF), Italy), Valter Bonvicini (National Institute for Nuclear Physics (INFN), Italy), and Jean in 't Zand (Netherlands Institute for Space Research (SRON), The Netherlands) for valuable discussions and help with specific requirements. The authors are also very grateful to Keith Gendreau (NASA Goddard Space Flight Center, Greenbelt, MD, USA), Adam Goldstein (Universities Space Research Association, Huntsville, AL, USA), Peter Jenke (University of Alabama in Huntsville, Huntsville, AL, USA), and Henric Krawczynski (Washington University in St. Louis, St. Louis, MO, USA).

This work was supported by NASA proposal number 22-APRA22-0026.

References

- 1 P. S. Ray, Z. Arzoumanian, S. Brandt, *et al.*, “STROBE-X: a probe-class mission for x-ray spectroscopy and timing on timescales from microseconds to years,” in *Space Telescopes and Instrumentation 2018: Ultraviolet to Gamma Ray*, J.-W. A. den Herder, S. Nikzad, and K. Nakazawa, Eds., *Society of Photo-Optical Instrumentation Engineers (SPIE) Conference Series* **10699**, 1069919 (2018).
- 2 P. S. Ray, Z. Arzoumanian, D. Ballantyne, *et al.*, “STROBE-X: X-ray Timing and Spectroscopy on Dynamical Timescales from Microseconds to Years,” *arXiv e-prints*, arXiv:1903.03035 (2019).
- 3 <https://strobe-x.org>.
- 4 P. S. Ray, P. W. A. Roming, *et al.*, “STROBE-X Mission Overview,” *J. Astron. Telesc. Instrum. Syst.* **VV**, PPP (2024).
- 5 K. C. Gendreau, Z. Arzoumanian, D. Maes, *et al.*, “The STROBE-X Low Energy Modular Array (LEMA) Instrument,” *J. Astron. Telesc. Instrum. Syst.* **VV**, PPP (2024).

- 6 A. L. Hutcheson, M. Feroci, A. Argan, *et al.*, “STROBE-X High Energy Modular Array (HEMA),” *J. Astron. Telesc. Instrum. Syst.* **VV**, PPP (2024).
- 7 R. Remillard, M. Hernanz, J. in ’t Zand, *et al.*, “The STROBE-X Wide Field Monitor Instrument,” *J. Astron. Telesc. Instrum. Syst.* **VV**, PPP (2024).
- 8 E. Gatti and P. Rehak, “Semiconductor drift chamber — An application of a novel charge transport scheme,” *Nuclear Instruments and Methods in Physics Research* **225**, 608–614 (1984).
- 9 A. Vacchi, A. Castoldi, S. Chinnici, *et al.*, “Performance of the UA6 large-area silicon drift chamber prototype,” *Nuclear Instruments and Methods in Physics Research A* **306**, 187–193 (1991).
- 10 R. Campana, G. Zampa, M. Feroci, *et al.*, “Imaging performance of a large-area Silicon Drift Detector for X-ray astronomy,” *Nuclear Instruments and Methods in Physics Research A* **633**, 22–30 (2011).
- 11 A. Rachevski, G. Zampa, N. Zampa, *et al.*, “Large-area linear Silicon Drift Detector design for X-ray experiments,” *Journal of Instrumentation* **9**, P07014 (2014).
- 12 G. De Geronimo and P. O’Connor, “MOSFET Optimization in Deep Submicron Technology for Charge Amplifiers,” *IEEE Transactions on Nuclear Science* **52**, 3223–3232 (2005).
- 13 G. De Geronimo, A. D’Andragora, S. Li, *et al.*, “Front-End ASIC for a Liquid Argon TPC,” *IEEE Transactions on Nuclear Science* **58**, 1376–1385 (2011).
- 14 G. De Geronimo, W. Chen, J. Fried, *et al.*, “Front-End ASIC for High Resolution X-Ray Spectrometers,” *IEEE Transactions on Nuclear Science* **55**, 1604–1609 (2008).
- 15 G. De Geronimo and S. Li, “Shaper Design in CMOS for High Dynamic Range,” *IEEE Transactions on Nuclear Science* **58**, 2382–2390 (2011).
- 16 G. De Geronimo, P. O’Connor, and J. Grosholz, “A CMOS baseline holder (BLH) for readout ASICs,” *IEEE Transactions on Nuclear Science* **47**, 818–822 (2000).
- 17 G. De Geronimo, J. Fried, S. Li, *et al.*, “VMM1—An ASIC for Micropattern Detectors,” *IEEE Transactions on Nuclear Science* **60**, 2314–2321 (2013).
- 18 G. De Geronimo, P. O’Connor, and A. Kandasamy, “Analog CMOS peak detect and hold circuits. Part 2. The two-phase offset-free and derandomizing configuration,” *Nuclear Instruments and Methods in Physics Research A* **484**, 544–556 (2002).
- 19 G. De Geronimo, “Low noise electronics for radiation sensors,” in *Medical Imaging: Principles, Detectors and Electronics*, K. Iniewski, Ed., John Wiley & Sons, Inc. (2009).
- 20 T. Calin, M. Nicolaidis, and R. Velazco, “Upset hardened memory design for submicron CMOS technology,” *IEEE Transactions on Nuclear Science* **43**, 2874–2878 (1996).
- 21 Z. Hu, Z. Liu, H. Shao, *et al.*, “Comprehensive Study on the Total Dose Effects in a 180-nm CMOS Technology,” *IEEE Transactions on Nuclear Science* **58**, 1347–1354 (2011).

Gianluigi De Geronimo is an adjunct professor with the University of Michigan and with the Stony Brook University, and a consultant. He received his MS and PhD degrees in Electronics and Communications from Milan Polytechnic. He is the author of more than 120 journal papers and one book chapter. His current research interests include low-noise front-end ASIC design and characterization. He is member of IEEE and editor for IEEE TNS.

Paul S. Ray is an astrophysicist at the U.S. Naval Research Laboratory. He received his A.B. in physics from the University of California, Berkeley in 1989 and his Ph.D. in physics from Caltech in 1995. His current research interests include multiwavelength studies of pulsars and other neutron star systems and X-ray instrument and mission development. He is a member of AAS, IAU, and Sigma Xi.

Eric A. Wulf is a research physicist with the Naval Research Laboratory. He received his MS degree in Physics from the University of Virginia and his PhD degree in Physics from the Duke University. He is the author of more than 110 journal papers. His current research interests include data acquisition and nuclear physics detectors. He is member of IEEE and of the American Astronomical Society.

Colleen Wilson-Hodge is an astrophysicist at NASA's Marshall Space Flight Center. She received her MS degree in 1996 and PhD degree in 1999. Both degrees were in Physics from the University of Alabama in Huntsville. Her current research interests include multimessenger transients along with X- and gamma-ray instrument and mission development. She is a member of AAS and IAU.

Biographies and photographs of the other authors are not available.